ELSEVIER

Contents lists available at ScienceDirect

### Quaternary Geochronology

journal homepage: www.elsevier.com/locate/quageo





## A quantitative assessment of snow shielding effects on surface exposure dating from a western North American <sup>10</sup>Be data compilation

Shan Ye<sup>a,\*</sup>, Joshua K. Cuzzone<sup>b</sup>, Shaun A. Marcott<sup>a</sup>, Joseph M. Licciardi<sup>c</sup>, Dylan J. Ward<sup>d</sup>, Jakob Heyman<sup>e</sup>, Daven P. Quinn<sup>a</sup>

- <sup>a</sup> University of Wisconsin-Madison, Department of Geoscience, 1215 W Dayton St., Madison, WI, 53705, USA
- b University of California, Los Angeles, Joint Institute for Regional Earth System Science & Engineering, Young Hall, Los Angeles, CA, 90095, USA
- University of New Hampshire, Department of Earth Sciences, 56 College Road, 214 James Hall, Durham, NH, 03824, USA
- <sup>d</sup> University of Cincinnati, Department of Geosciences, 502 Geology-Physics, Cincinnati OH, 45221, USA
- e University of Gothenburg, Department of Earth Sciences, Box 100, 405 30, Gothenburg, Sweden

#### ARTICLE INFO

# Keywords: Cosmogenic nuclide dating Alpine glaciers Cosmogenic database Western United States and Canada Snow reanalysis Pleistocene glaciation

#### ABSTRACT

To better assess the spatiotemporal variations of the snow shielding effect on surface exposure dating, we compiled a dataset of 1341 10Be ages from alpine moraines and glacially eroded valleys across western North America, and conducted a sensitivity test with both modern and time-integrated snow data covering the same region. Our analyses reveal significant differences in snow shielding both across our geographic domain and through time. In our time-integrated experiments we find snow-based exposure age corrections as low as 3.5% in the Great Basin region and high as 28.4% in the Pacific Northwest for samples dating to the Last Glacial Maximum (LGM) when no wind-sweeping is assumed. As demonstrated with our time-varying snow conditions with a global climate model and a positive degree day model, modern snow conditions across western North America cannot account for the varying snow patterns under large scale climate shifts since the LGM. The snowbased exposure age corrections from the modern data differ from those calculated by our time-varying model by up to 17% across our model domain. In addition, we find that the <sup>10</sup>Be ages calculated under two end-member scenarios regarding wind-sweeping effects, specifically whether boulders were shielded only when the total snow accumulation exceeded boulder heights or were always shielded when the snow was present, can differ by ~7.6% on average for LGM aged samples. Our analyses provide a model-based estimates of the spatiotemporal variability and complexity of snow shielding effects on surface exposure dates across western North America and highlight the need to consider snow depth variations both spatially and temporally when conducting surface exposure dating in terrains where snowfall accumulation is significant.

#### 1. Introduction

Cosmogenic nuclide surface exposure dating is a widely-applied tool in geochronology. Different cosmogenic nuclides have been measured in a variety of minerals and rocks, such as <sup>3</sup>He and <sup>21</sup>Ne in olivine or pyroxene, <sup>26</sup>Al and <sup>10</sup>Be in quartz, and <sup>36</sup>Cl in silicate or carbonate rocks, to estimate the amount of time a surface has been exposed to cosmic rays (Ivy-Ochs and Kober, 2008). Among these isotopes, <sup>10</sup>Be is the most widely applied and is generally used on quartz-bearing rocks which are very common on the Earth surface. The 1.39-Myr half-life (Nishiizumi et al., 2007; Chmeleff, 2010; Korschinek, 2010) and relative simplicity of sample processing and production pathways make <sup>10</sup>Be a suitable tool

to date geologically young surfaces (Brown 1987; Morris 1991), and thus <sup>10</sup>Be has been a popular geochronometer in the studies of glaciated landscapes worldwide for determining the history of the Quaternary glaciations (Balco, 2011). In western North America, surface exposure dating with <sup>10</sup>Be has been applied on bedrock and moraine boulders to determine former glacier positions and infer past climate conditions (e. g., Gosse et al., 1995a; Phillips et al., 1997; Hancock et al., 1999: Dahms 2004; Refsnider et al., 2008; Rood et al., 2011; Dahms et al., 2018; Marcott et al., 2019; Schweinsberg et al., 2020; Laabs et al., 2020).

The production rate of cosmogenic <sup>10</sup>Be at Earth's surface varies in space and time because of variations in the geomagnetic field and atmospheric pressure, both of which change with latitude, altitude, and

E-mail address: shan.ye@wisc.edu (S. Ye).

<sup>\*</sup> Corresponding author.

time (Lal and Peters, 1967; Lal, 1991; Lifton et al., 2005; Balco et al., 2008). Thus, a geographic and temporal scaling is required in the age calibration (Nishiizumi et al., 1989). However, the effects of many geological (e.g., erosion and isostatic rebound) and climatological (e.g., snow cover) processes on surface exposure ages, which also have spatial variations, are not explicitly quantified and incorporated into common age calculations. For example, steep climatologic gradients across a complex mountainous terrain, such as that in western North America, can influence <sup>10</sup>Be ages by imposing variable snow shielding across the space; these spatial variations of snow shielding have not been systematically assessed at continental scales and the relatively few exposure-age studies that applied snow corrections have generally relied on modern regional-scale climatological data or other site-specific assumptions (e.g. Licciardi et al., 1999; Licciardi et al., 2001; Benson et al., 2004; Hormes et al., 2008; Hippolyte et al., 2009; Delunel et al., 2014; Hippe et al., 2014; Margold et al., 2014; Chenet et al., 2016). However,

the vast majority of studies do not apply a snow correction and either assume that the local snow shielding is insignificant, which is plausible based on modern snowpack data and/or assumptions of snow wind-sweeping of boulder surface, or posit that snow shielding effects are within the uncertainties of the age calculation itself (e.g., Phillips et al., 2006; Dubé-Loubert et al., 2018; Marcott et al., 2019). How and whether to apply a snow correction for any particular set of surface exposure ages is therefore important, both for robust data interpretation and for providing more confidence in the method itself.

Here, we compile a dataset of 1341 <sup>10</sup>Be ages from alpine moraine ridges across the western North America (Fig. 1), which are archived in the newly developed Sparrow Database (https://sparrow-cosmo.geoscience.wisc.edu/). We use this compiled dataset, along with modern snow reanalysis data and computer-simulated historical snow data (TraCE-21ka), to quantitatively illustrate the significance of snow shielding on <sup>10</sup>Be-based ages from bedrock and boulders samples for

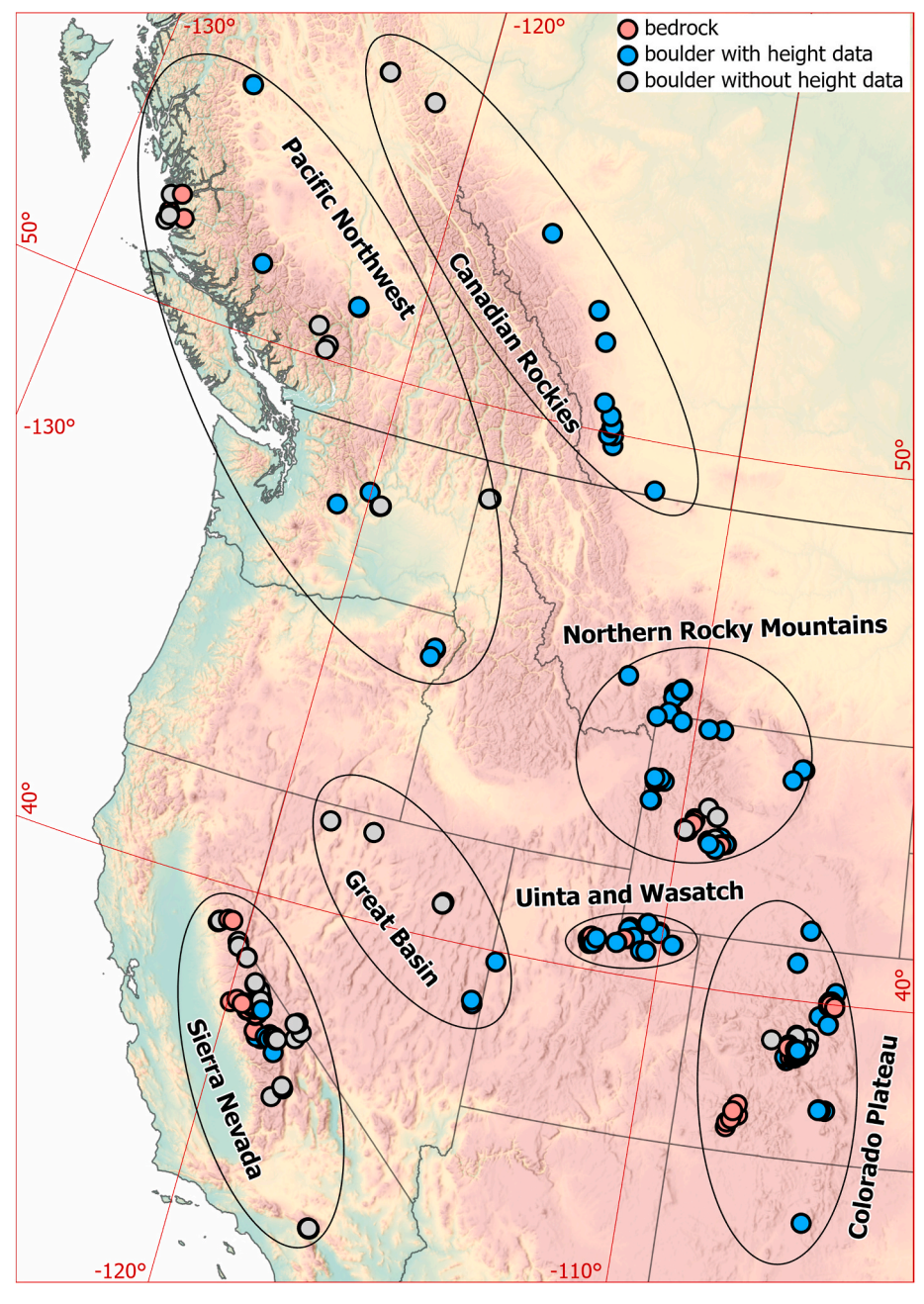


Fig. 1. Map showing the location of all samples in this data compilation and the ranges of general geographic regions. Names correspond to descriptions in text.

constraining past glacial and climate histories. Our study focuses on  $^{10}$ Be and should generally apply to other nuclides with spallation-dominated production, but does not address the slower production pathways, such as those associated with  $^{36}$ Cl, which have a more complicated accumulation paths in rocks and require more complex modeling when snow is present.

#### 2. Data and methods

Our  $^{10}$ Be dataset is based on a global synthesis (Heyman et al., 2016) and newly archived data and metadata as part of this study; metadata include geographic coordinates, elevations, sampling material, published ages, and other sample and site-specific information (Table 1). For the purposes of this paper, we spatially limit this synthesis to the western

**Table 1**Original publications that contributed to this data compilation, and the number of samples from each study.

Publication	Samples	Publication	Samples	Publication	Samples
Amos et al. (2010)	6	Gosse et al. (1995a)	16	Menounos et al. (2013)	6
Balbas et al. (2017)	8	Gosse et al. (1995b)	37	Menounos et al. (2017)	6
Becker et al. (2018a)	20	Guido et al. (2007)	7	Munroe et al. (2006)	21
Becker et al. (2018b)	36	Howle et al. (2012)	4	Nishiizumi et al. (1993)	11
Benn et al. (2006)	13	Kohut (2011)	20	Owen et al. (2003)	51
Benson et al. (2004)	5	Laabs and Munroe (2016)	14	Phillips et al. (1997)	10
Benson et al. (2007)	25	Laabs et al. (2007)	13	Pierce et al. (2017)	16
Breckenridge and Phillips (2010)	5	Laabs et al. (2009)	27	Quirk et al. (2018)	17
Briner (2009)	22	Laabs et al. (2011)	24	Quirk et al. (2020)	22
Brugger (2007)	7	Laabs et al. (2013)	28	Refsnider et al. (2008)	16
Brugger et al. (2019a)	17	Laabs et al. (2020)	38	Rood et al. (2011)	102
Brugger et al. (2019b)	10	Leonard et al. (2017)	32	Ruleman et al. (2018)	9
Dahms et al. (2018)	48	Licciardi and Pierce (2008)	71	Schaefer et al. (2006)	4
Darvill et al. (2018)	32	Licciardi and Pierce (2018)	6	Schildgen (2000)	5
Dühnforth and Anderson (2011)	15	Licciardi et al. (2001)	43	Schweinsberg et al. (2020)	35
Dühnforth et al. (2010)	28	Licciardi et al. (2004)	29	Tranel and Strow (2017)	2
Dulfer et al. (2021)	8	Mahan et al. (2014)	1	Tranel et al. (2015)	5
Egli et al. (2020)	8	Marcott et al. (2019)	134	Tulenko et al. (2020)	12
Fabel et al. (2004)	22	Margold et al. (2014)	8	Ward et al. (2009)	19
Fleming (2019)	17	Margold et al. (2019)	16	Wesnousky et al. (2016)	37
		•		Young et al. (2011)	11

United States and western Canada which results in 1341 individual dated samples (more than 80% have an age between 8 ka and 26 ka), among which 172 are from bedrock derived samples, 15 are from cobble to pebble sized materials, and 1154 are from glacially transported boulders. We recalculated all of the <sup>10</sup>Be ages using the online cosmogenic age calculator (v.3) (Balco et al., 2008) for each of the three commonly used scaling factors (i.e. St, Lm, and LSDn). Of the boulder samples, we also compiled boulder height data for 697 samples. These samples are generally grouped into seven clusters differentiated by geography: the Pacific Northwest, Canadian Rockies, Northern (U.S.) Rocky Mountains, Sierra Nevada, Great Basin, Uinta and Wasatch Ranges, and Colorado Plateau (Fig. 1).

Modern monthly snow water equivalent (SWE) data were derived for years between 1998 and 2020 and retrieved from the Canadian Meteorological Centre (CMC) Daily Snow Depth Analysis Data Version 1 (Brown and Brasnett, 2020), which provides snow reanalysis data covering the entire Northern Hemisphere at a spatial resolution of 24 km × 24 km. This dataset contains monthly mean snow depth and estimated SWE at each grid point. The monthly mean snow depth is calculated from the daily snow depth data in the same database, and the daily depth is derived from real-time in-situ daily snow depth observations with an interpolation based on a snow model of analyzed temperatures and forecast precipitation (Brasnett, 1999). The monthly SWE between October and June is determined by the snow depth and the estimated snow density based on the empirical Northern Hemispheric snow classes from Sturm et al. (1995), which assign snow densities based on the month and geographic settings (tundra, taiga, maritime, ephemeral, prairie, and alpine).

The snow correction factor (F) of each <sup>10</sup>Be sample (Gosse and Phillips, 2001) is calculated by:

$$F = \frac{1}{12} \sum_{1}^{n} e^{\frac{-p_{u} \cdot \text{SWE}}{\Lambda}} \tag{1}$$

where  $\rho_w$  is the water density (1 g/cm<sup>3</sup>), n is the month,  $\Lambda$  is the spallogenic neutron attenuation length for which we assume as  $160 \text{ g/cm}^2$  in this study (Gosse and Phillips, 2001), and SWE is the snow water equivalent data (in cm) retrieved from the CMC dataset (Brown and Brasnett, 2020). The SWE data are integrated for each month at each grid space, and interpolated across the space by the inverse distance weighting (IDW) method in ArcGIS Pro, and are then assigned to samples in the  $^{10}$ Be dataset by the geographic coordinate.

In order to reconstruct historical snow depth from 22,000 years ago to present, we use a downscaled climate model product for North America from Lorenz et al. (2016), which relies on the coarser TraCE-21ka simulations (Liu et al., 2009; He, 2011). For this analysis we use monthly mean air temperature (2-m) and precipitation, which is provided on a 0.5° grid. Because snow depth is neither explicitly modeled nor a direct output from the climate model, we use a common approach to calculate snow depth from the model output using air temperature and precipitation (Krasting et al., 2013). First, we calculate the fraction of monthly precipitation falling as snow as a function of temperature (Cehak-Trock, 1957; Legates, 1987; Rawlins et al., 2006):

$$f = \frac{1}{1.0 + 1.61 \times (1.35)^T} \tag{2}$$

Here, f is the monthly mean fraction of total precipitation that falls as snow, and is based on the mean air temperature, T (in  $^{\circ}$ C). We apply this fraction to the monthly mean precipitation from the climate model output (Lorenz et al., 2016) to derive the snow depth equivalent back to 22,000 years ago at 500-year time intervals with an assumed constant 10:1 snow-to-liquid ratio. We assume the climatological condition before the LGM was similar to the LGM condition, so for samples older than 22,000 years (n = 273, among which 207 are older than 30,000 years), the output at 22,000 years ago is used for the duration before the LGM. Note that the climate model does not calculate snow depth beyond

2 m (Krasting et al., 2013), nor does it consider the snow melting. Hence for this study, we instead estimate snow accumulation based on the modeled precipitation and the assumed melting based on a Positive Degree Day (PDD) model (Blard et al., 2007). We calculate the monthly snow melt (M) by:

$$M = T_{pos} * DDF (3)$$

where  $T_{pos}$  is the monthly mean of the daily maximum positive temperature (°C) derived from the climate model output and DDF is the snow's degree day factor. For this analysis we apply the monthly mean of the daily maximum positive temperature that is derived by averaging the model minimum and maximum temperatures with an imposed daily cycle about the mean. We then integrate across all positive temperatures for each month to derive the daily maximum positive temperature. Applying the monthly mean maximum temperature in the PDD model likely overestimates the melt in our methodology, but we prefer this to using, for instance, the monthly mean temperature which clearly underestimates melt since below-freezing temperatures are still retained across much of the summer months.

For this analysis we use 100 mm/°C/month for the snow *DDF* (Hock, 1999, 2003). For each year (time snap) in the time series, the snow starts to accumulate in September, and the monthly snow depth is calculated

bv:

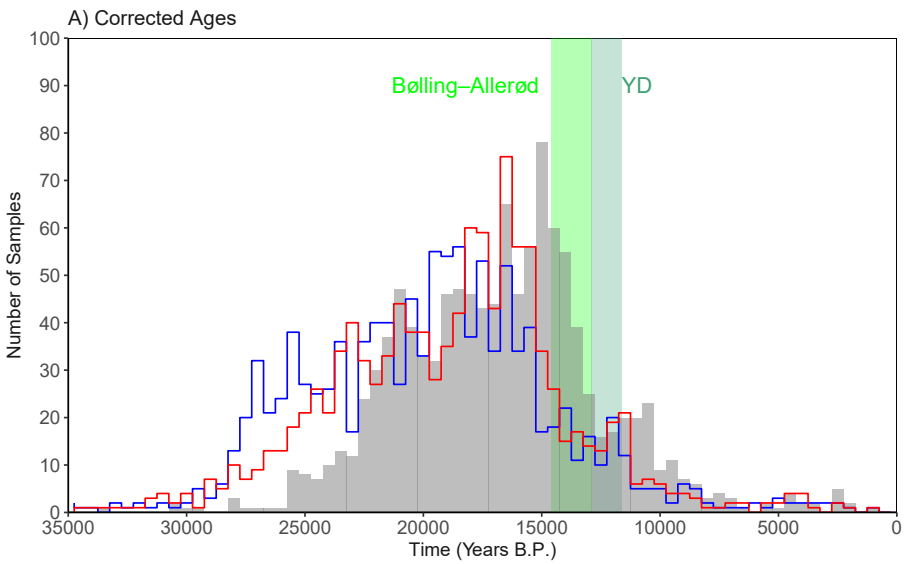
$$h_{n (i)} = h_{n (i-1)} + P * f_{(i)} - M_{(i)}$$
(4)

where P is the total precipitation, f is the monthly mean fraction of total precipitation that falls as snow calculated in Eq. (2), M is the monthly melt, and i indicates the month. We assumed 0 snow accumulation in summer months (June, July, and August), or any other months that resulted in a negative  $h_n$  value. For the time-integrated snow data and PDD modeling, we calculated the snow correction factor (F) by:

$$F = \frac{1}{12} \sum_{1}^{n} e^{\frac{-\rho_n \cdot h_n}{\lambda}} \tag{5}$$

where  $\rho_n$  is the snow density,  $h_s$  is the snow depth (as calculated in Eq. (4)), and other parameters are same as in Eq. (1). We set the snow density to be 0.25 g/cm<sup>3</sup> based on the mean of modern snow data (Brown and Brasnett, 2020) and SNOTEL data in our study area (see the sensitivity test with SNOTEL below).

The snow depth parameter  $(h_n)$  in Eq. (5) applied in our calculations is assumed to be equivalent to the local snow depth for the bedrock to cobble-sized samples but varies for the boulder samples depending on how we consider the influence of boulder heights above the local



B) Corrected Ages (wind-swept) 100 90 Published Ages 80 Snow Data 70 modern Number of Sample: 60 time-integrated 50 40 30 20 10 35000 25000 20000 15000 10000 Time (Years B.P.)

Fig. 2. Distribution of ages in this study before and after applying snow correction factors. A) The distribution of ages after applying the snow correction factor for modern snow (red) and the time-integrated snow (blue) data, both without considering wind sweeping. Gray bins are recalculated ages from published sample metadata under the LSDn scaling factor (Balco et al., 2008). B) Same as A but considering the effects of wind sweeping. Green vertical bars demarcate the Bølling-Allerød and Younger Dryas (YD) periods.

landscape. We partition the snow shielding scenarios as two endmember states regarding boulder heights. The first scenario is that the snow accumulation is considered 'wind-swept' on top of the boulders (Ivy-Ochs et al., 1999) and that the boulders were only shielded when the total snow accumulation exceeded boulder height. In this scenario, snow depth used in the calculation is zero when the boulder height is taller than the local snow depth and is the difference between the boulder height and the local snow depth when the boulder is smaller than the local snow depth. The second scenario is that snow depths on top of boulders are equal to local snow depths, which means the boulder heights will not influence the snow correction factor. Thus, boulder heights are ignored for this scenario and the local snow depth data, as they are for the bedrock to cobble sized samples, are used in the snow correction calculation.

The snow correction factor (F) indicates how much the <sup>10</sup>Be age has been shifted by the snow shielding. A higher snow correction factor means a lower degree of snow shielding, and a snow correction factor of 1 indicates totally snow free and thus no shifting of age by snow.

Snow-corrected ages ( $A_{snow}$ ) for all samples (Fig. 2) are calculated by:

$$A_{snow} = \frac{A}{F} \tag{6}$$

where A is the sample exposure age derived from the online cosmogenic calculator (v.3) (Balco et al., 2008) and F is the snow correction factor. This calculation is a simplification and assumes spallation is the only production pathway.

The time-integrated snow correction factor is then calculated using Eq. (5) for all samples by using the reconstructed historical snow depth and assuming the contemporary climatological snow density for each month across the time domain. The gridded snow correction factor is calculated at 500-year timesteps back to 22,000 years ago, and for each geographical region in our study we show the mean snow correction factor time series and corresponding standard deviations (Fig. 3).

#### 3. Results

The mean elevation of all 1341 bedrock and boulder samples in our synthesis is approximately 2495 m above the sea level, and the elevation range of all samples is from 36 to 3871 m. The range of sample latitude is between 31.0°N and 56.5°N. Among them, 774 samples have a latitude between 37.0°N and 41.0°N, while 390 more samples are distributed between 41.0°N and 47.0°N. The average boulder height is 127 cm ( $\pm 82$  cm, 1 sd) for the 695 moraine boulder samples with known heights. On average the boulders are 104 cm above the reconstructed local, modern March snow depth, and approximately 5% of those boulders are smaller than the local March snow height.

Snow density and snow depth generally vary spatially as a function of latitude and altitude, and vary temporally as a function of seasonal changes and large-scale shifts in climate since the LGM. Higher latitude and higher altitude locations usually have deeper snow accumulation under the modern setting, while in the summer months (July-September) most of our study area does not have snow coverage. The Northern Rocky Mountains have the thickest snow in February (mean/ min/max: 36.5, 6.8, and 98.4 cm) among all sample locations based on the modern snow data, followed by the Pacific Northwest (36.4, 3.4, and 108.9 cm), the Sierra Nevada (32.1, 2.6, and 70.4 cm), and the Canadian Rockies (24.7, 2.5, and 66.2 cm). These regions thus have large amounts of snow shielding which influence their respective cosmogenic exposure ages. Compared to other sites, the Great Basin lies in a climatological precipitation shadow where the mean snow thickness of February at all sample locations is only 4.9 cm (min/max: 1.5 and 5.9 cm). The Colorado Plateau, Uinta and Wasatch regions have intermediate snow depths among site locations in this study (mean values are between 15 and 20 cm) because they are farther from an ocean moisture source, located at

higher elevations, and are outside any major rain shadow while receiving some local moisture recharge from more proximal sources such as the Great Salt Lake.

There are also spatial variations in snow density among the general regions. Based on our modern snow data, the Colorado Plateau, Northern Rocky Mountains, and Sierra Nevada sites generally have higher snow density at sample locations, which means that in these regions the annual durations of snow coverage are likely longer and thus increase the snow shielding. Within each region, the snow density and depth vary with physical geographic properties, including the elevation, slope aspect, and local rain shadowing. For example, in the Sierra Nevada, our data show that the snow density has a sharp gradient on the western face of the range and a gradual gradient on the eastern face.

The spatiotemporal variation in the time-integrated paleo-snow data shows a general south to north shift in the zone of greatest snow accumulation through time (Fig. 5). During the LGM the mean position of wintertime snow is pushed further to the south where the Colorado Plateau, Uinta and Wasatch, Great Basins, and Sierra Nevada received more snow than the present (locally >500 cm in November), while the Canadian Rockies and the inland half of the Pacific Northwest regions had thinner snow coverages. During the Younger Dryas (YD) cold interval (12.9–11.5 ka), sites in Canada began to accumulate more snow while in the southern part of our study area the depth of snow began to decrease. By the mid Holocene (5 ka) the snow depth in the Colorado Plateau dropped close to its current level.

Assuming snow accumulation is wind-swept on top of the boulders and boulders were only shielded when the total accumulation exceeded boulder height, the mean snow shielding adjustment for all samples is 5.9% (modern snow data) or 13.4% (time-integrated data) across western North America. If the boulders are not wind-swept, then the snow depths on top of boulders would be equal to the local snow depth, making the mean snow shielding adjustment for all samples 12.1% (modern snow data) or 17.1% (time-integrated data). Our sample locations have diverse geographical setting in terms of latitude, topography, and the proximity to the ocean. To better assess how the snow shielding effect changes across these geographic settings and where samples with higher or lower snow correction factors are clustered, we apply the Getis-Ord Gi\* analysis, a statistical method for identifying high-value and low-value clusters in spatial data (Getis and Keith Ord, 2010). Based on our analyses, clear spatial patterns can be observed as higher and lower snow correction factors (Fig. 4). The Sierra Nevada generally has lower snow correction factors which indicate a relatively higher level of snow shielding compared to the full spatial domain, while the Canadian Rockies and Great Basin regions have higher snow correction factors which indicate a relatively lower level of snow shielding. The Uinta and Wasatch region has lower snow correction factors in the time-integrated snow data and has higher snow correction factors in the modern snow data (Table 2). When boulder heights are ignored with respect to snow cover and the time-integrated snow data are considered, the uppermost bounds of snow shielding within our study area are reached and shift to the lower correction factors (more snow shielding effects) across most of the domain. For the Uinta and Wasatch region the change is the most significant (0.92 to 0.82 for Uinta and Wasatch region, and 0.89 to 0.86 for all data) and thus this region changed from relatively higher snow correction factors under the modern snow data into a relatively lower value under the time-integrated snow data.

Adjusted sample ages are calculated based on the snow correction factors for each region under four scenarios: 1) not wind-swept under modern snow data, 2) wind-swept under modern snow data, 3) not wind-swept under time-integrated snow data, and 4) wind-swept under time-integrated snow data (Fig. 2). The snow correction amount for LGM-aged samples (whose ages are between 23 and 18 ka) are provided in Table 2. On average the LGM-based samples are approximately 2480 or 3550 years older (modern and time-integrated snow data, respectively) than their published ages when not wind swept, and 1370 and

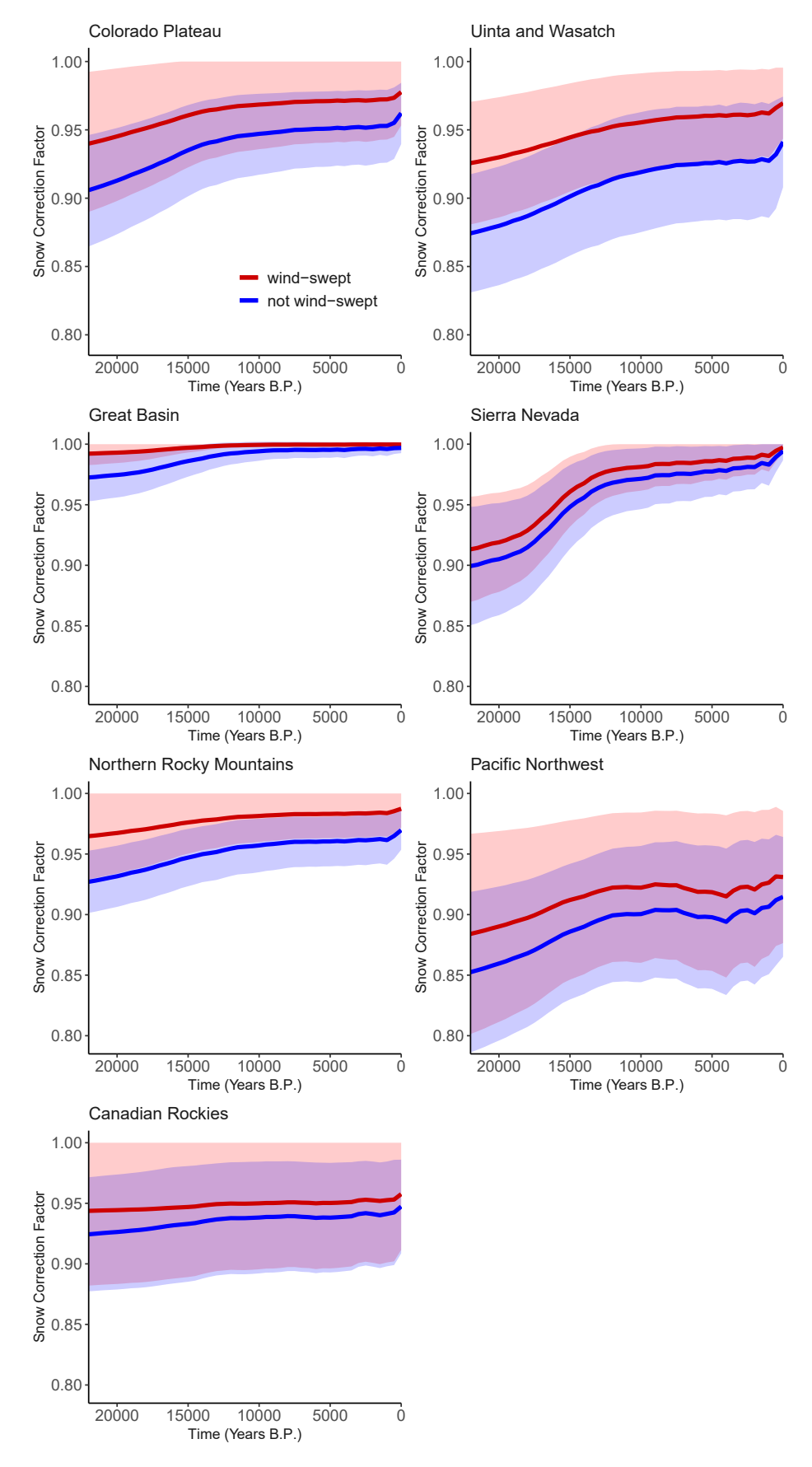


Fig. 3. Time series of mean snow correction factor (time-integrated) from LGM to the present in each general region and their first standard deviations.

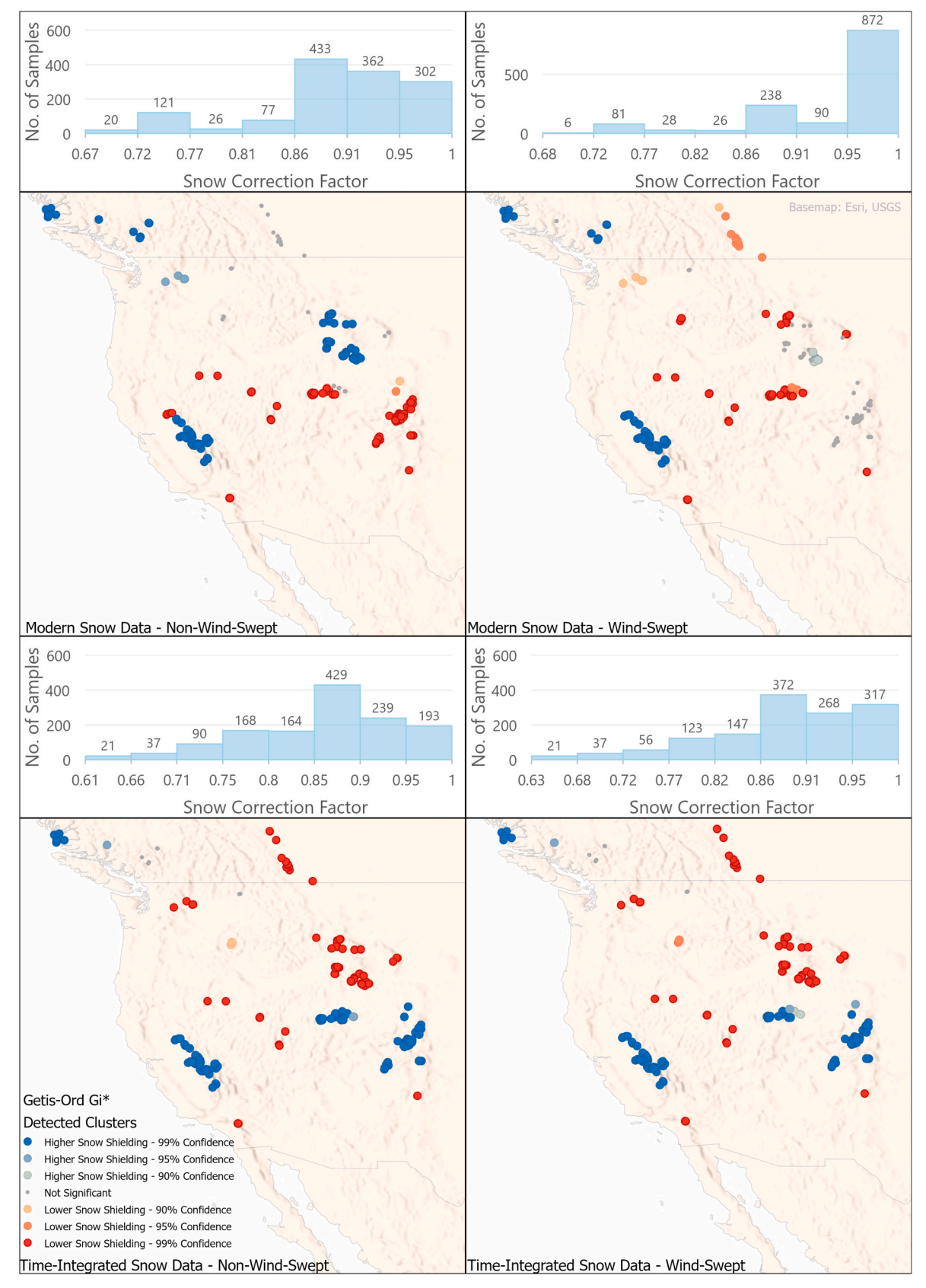


Fig. 4. Clusters of samples with higher and lower snow shielding detected by the Getis-Ord Gi\* test under different scenarios. Blue colors indicate lower values in the snow correction factors which indicates larger amounts of shifting in the age by snow shielding. Red colors indicate higher values in the snow correction factors which indicates smaller amounts of shifting in the age by snow shielding. Histograms show the distribution of snow factors under each scenario.

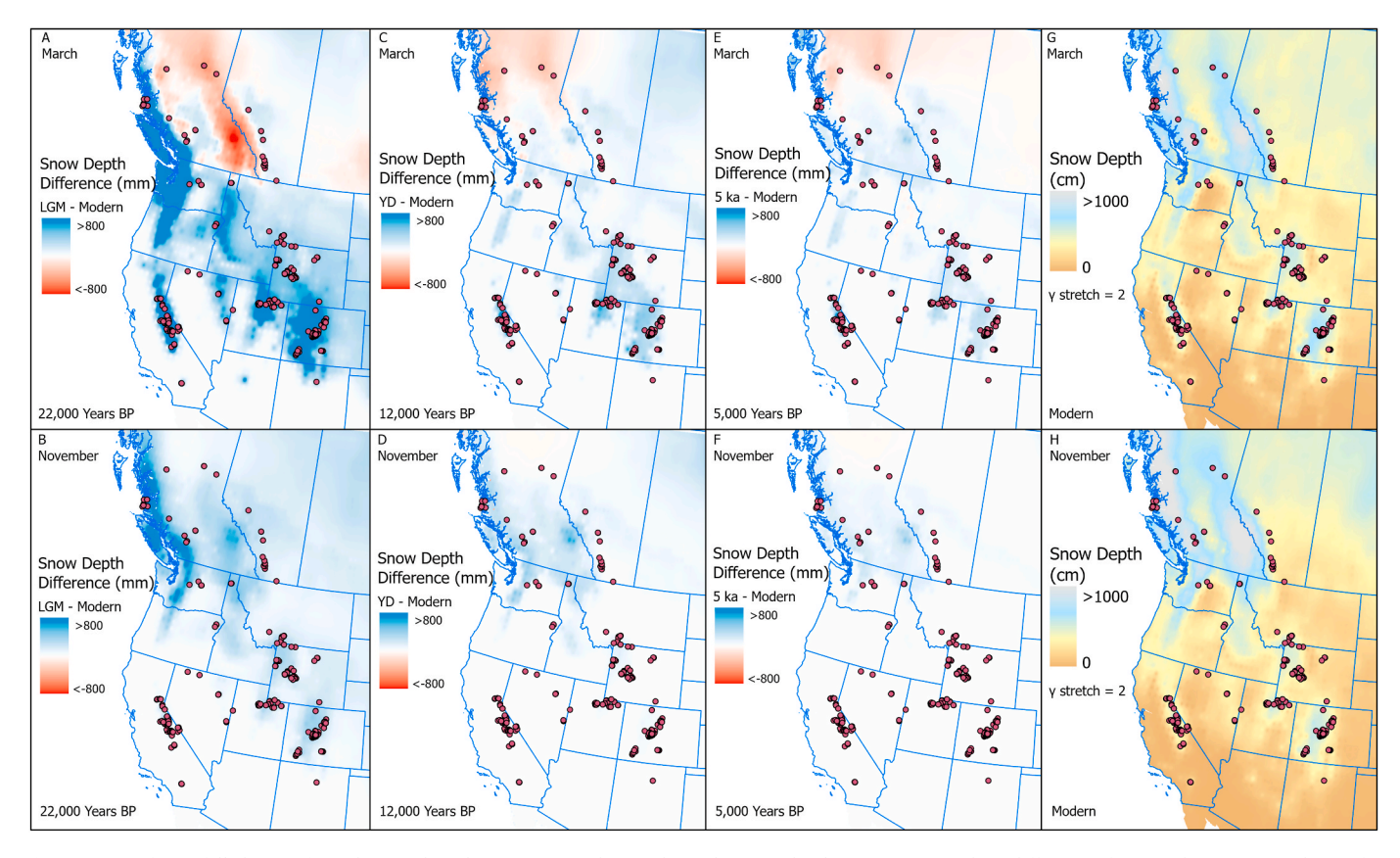


Fig. 5. Maps of snowfall changes from the PDD-based time-integrated snow data. The snow depths maps (A to F) show differences from modern snow conditions for the spring and fall seasons for time slices at the LGM (22 ka), Younger Dryas (12 ka), and mid-Holocene (5 ka). Red colors are lower snow depth compared to the modern snow and blue colors are higher snow depth. Modern snow depths are shown in G and H for comparison. Note: snow depth difference maps (A to F) are in millimeters and snow depth maps are in centimeters (G and H).

2790 years older when wind-swept on top of the boulders. Variations can be observed across different general regions, through space and time. On average the Great Basin has the smallest amount of snow correction, which can be explained by the small amount of snow accumulation in that region both for the modern conditions and in the climate model simulated estimates. The Pacific Northwest has the greatest amounts of snow age correction, which can be explained by its proximity to the Pacific Ocean (i.e. the moisture source) and higher elevation. The Sierra Nevada has the second highest amounts of snow age correction for these same reasons despite its lower latitude.

#### 4. Discussion

Previous studies have suggested the importance of quantifying snow shielding and its influence on the age calculation of cosmogenic surface exposure dating. Prior studies such as Schildgen et al. (2005) found that in Scotland snow shielding can reduce the long-term nuclide production rate by 12%–14% at altitudes as low as only 900 m. Delunel et al. (2020) presented a snow shielding model for <sup>10</sup>Be production rates based on a data compilation in French and Swiss Alps, and found a negative correlation between the snow shielding factor and catchment elevation. In the western United States, Benson et al. (2004) utilized effective wetness as a proxy to reconstruct the snow shielding factor in north-central Colorado and found snow shielding to be potentially responsible for as much as 48% of the discrepancies between cosmogenic nuclides ages and their expected ages based on existing knowledge of past climate histories. In some instances, local-scale corrections have been applied to <sup>3</sup>He and <sup>10</sup>Be data based on modern snow surveys and applied through time to account for snow shielding effects (Licciardi et al., 2001). Here we provide a more comprehensive snow shielding analysis for the

western United States and Canada and extend the work from prior studies (e.g. Licciardi et al., 1999) to a wider geographic area and temporal ranges through the incorporation of modern snow reanalysis and simulated historical climate data.

We calculated the percentage of ages shifted by the snow shielding for all the LGM samples (ages between 23 and 18 ka) in our dataset (Table 2). On average, ages of all LGM samples in the compilation are shifted by about 17.2% under the time-integrated snow data without considering the wind-sweeping. This illustrates that snow shielding can significantly influence the <sup>10</sup>Be ages in western North America when considering variations in historical snow depth. There is no clear correlation between the modern snow shielding and elevation (Pearson correlation coefficient = 0.03, single-predictor regression  $R^2 < 0.01$ ) or latitude (correlation coefficient = 0.15,  $R^2 = 0.02$ ), but we find that the heterogeneity of snow shielding exists between different geographical regions. For example, ages of LGM samples in the Sierra Nevada region are shifted by about 17.8% on average under the time-integrated snow data without considering the wind-sweeping, which demonstrates that the snow effect is high in this region while those in the Great Basin are only shifted by 3.5% on average under the same scenario, which demonstrates that the snow effect is relatively low.

In addition to spatial heterogeneity, our recalculated ages of LGM samples reveals temporal variation of snow factors in our study area. For instance, LGM sample ages in the Great Basin are shifted by less than 1% under the modern snow data but shifted by 3.5% under the time-integrated snow data when no wind-sweeping is assumed. This is because the Great Basin region received more snow during the LGM and the last deglaciation compared to the modern climatology (Figs. 3 and 5). Five of the seven regions have larger snow corrections for LGM samples under the time-integrated snow data than under the modern

The difference in years (rounded to the nearest decade) between ages with and without the consideration of snow shielding factors for all LGM (23-18 ka) samples. LGM<sub>H</sub> are number of samples where boulder height

measurements are available. Total number of samples from each location are also included

Snow Data	Modern	Modern Snow Date	,						Time in	ime integrated Cnow Data	now Data						(u) M51	I CM. (n)	Total (n)
SIOW Data	MODELII	SHOW Dat	ומ						III-DIIII	icgiaica s	IIOW Data						roin (II)	(II) HIMIDT	TOTAL (III)
	Not Wind-swept	d-swept			Wind-swept	ept			Not Wir.	Vot Wind-swept			Wind-swept	/ept					
Scaling Factors	St	Lm	LSDn	LSDn Average	St	Lm	LSDn	Average	St	Lm	LSDn	Average	St	Lm	LSDn	Average			
Canadian Rockies	2410	2350	2280	2350	1190	1160	1110	1150	2030	1990	1920	1980	800	780	750	780	2	1	29
Colorado Plateau	2070	1980	1930	1990	1000	950	920	096	5190	4950	4830	4990	4250	4050	3950	4080	69	33	300
Great Basin	230	220	220	220	20	10	10	10	800	770	770	780	330	310	310	320	30	17	100
Northern Rocky Mountains	3400	3260	3200	3290	2030	1930	1880	1950	2410	2310	2260	2330	1460	1400	1370	1410	47	26	310
Pacific Northwest	4080	3990	3990	4020	2670	2630	2630	2640	5720	5590	5610	5640	4730	4630	4650	4670	18	10	94
Sierra Nevada	3540	3400	3460	3470	2410	2310	2350	2350	3830	3670	3720	3740	3230	3100	3140	3150	26	13	340
Uinta and Wasatch	1720	1650	1610	1660	40	40	40	40	4370	4200	4130	4230	3520	3380	3320	3400	41	40	168

snow data. The exceptions are the Canadian Rockies and Northern Rocky Mountains. This is likely related to the higher latitude and continental setting of these locations, where the moisture depletion related to the migration of jet stream during the retreat of the Laurentide Ice Sheet led to less snowfall (McGee et al., 2018; Lora and Ibarra, 2019; Amaya, 2022).

We also find that results can vary substantially when considering whether snow on top of boulders is considered wind-swept or not. Our analysis results in two end member scenarios regarding the windsweeping of snow (Table 2). While the site-specific environment is likely more complicated than our binary sensitivity test, the actual snow correction factors are likely being constrained between these two end members. For example, for the time-integrated snow data, LGM ages of Colorado Plateau samples are shifted by 23.2% when the non-windswept scenario is assumed and by 18.9% when the wind-swept scenario is assumed; ages for the Northern Rocky Mountains region are shifted by 10.9% when the non-wind-swept scenario is assumed and by 6.6% when the wind-swept scenario is assumed. Based on prior work by Heyman et al. (2016), which found that groupings of 'tall boulders' often vield older clustered exposure ages, it can be argued that the snow correction factor is closer to the wind-swept scenario. However, when applying the time-integrated snow data, the differences between wind-sweeping and non-wind-sweeping are generally reduced, because in most places the depth of the snow would have exceeded the heights of the boulders during the LGM, thus making it rare for the top of the boulder to be completely snow-free.

The spatial coverage and properties of snow are modeled to have changed through time (Collins et al., 2006), and the snow correction factor changes accordingly in our analyses (Fig. 5). Snow accumulation was higher than modern in the southern part western North America during the LGM (e.g., 22,000 years ago) because the jet stream was further south compared to present-day (Kutzbach 1987; Oster et al., 2015; Tulenko et al., 2020; Amaya, 2022). As a result, samples in the Sierra Nevada and Colorado Plateau generally experienced a higher level of snow shielding in the LGM and during the early phases of the last deglaciation (Fig. 3) before the jet stream migrated northward. The Pacific Northwest region also had higher snow shielding in the LGM mainly because of increased spatial winter snow coverage. The temporal variations in the snow accumulation and coverage in the Canadian and Northern Rocky Mountains are relatively minor in comparison, likely because of their more continental snow climate (i.e., greater distance from the ocean and rain shadow effect), resulting in reduced snowfall, even compared to what is estimated in the reanalysis data for the present day. Based on our analyses, the historical snow correction factors in these two general regions only have a gradual increase through time in the snow correction factor reflecting this phenomenon.

The spatiotemporal shifting of snow shown in our results (Fig. 5) is consistent with latitudinal shifts in the jet stream (Kutzbach, 1987). The jet stream was located further to the south 22,000 years ago than the present day, due to a combination of the thermal and mechanical forcing of the Laurentide Ice Sheet (Bromwich et al., 2004) and ocean-atmosphere feedbacks forced in part by ice sheet albedo (Amaya, 2022). Therefore, simulations of wintertime precipitation show a general increase for areas of southern Western North America (Bush and Philander, 1999), and are consistent with proxy records of precipitation (Oster et al., 2015). Following the LGM, the Laurentide Ice Sheet retreated further to the north with models demonstrating that the jet stream and general snowpack also shifted northward (Kutzbach 1987).

We compare our results to some previous snow shielding studies. Benson et al. (2004) found that snow shielding can shift ages of exposure dated Pinedale boulder samples (20.9–16.5 ka) by 12% in north-central Colorado. In our compilation, <sup>10</sup>Be ages from Colorado Plateau are shifted by 19% (not wind-swept) or 15% (wind-swept) for samples within the same temporal range. Gosse et al. (1995a) estimates that YD sample ages at Inner Titcomb Lakes moraine (Wind River, Wyoming) can be shifted by as much as 4% after considering snow effects. Our

compilation shows that in the similar region (Northern Rocky Mountains), near-YD sample ages (13–11 ka) are shifted by 13.0% (not wind-swept) or 3.3% (wind-swept). These estimations of snow shielding are within or close to the ranges bounded by snow and wind scenarios in our study but are closer to the wind-swept scenario which are consistent with what was inferred from Heyman et al. (2016) that snow correction factor is likely closer to the wind-swept scenario.

While our study presents a large-scale snow dataset when considering cosmogenic data in western Canada and the United States, we acknowledge that there are limitations of our analyses. The spatial and temporal resolutions of our snow data are not high enough to differentiate local variations in snow property at a specific location (i.e. subkilometer scale). For mountainous regions of western North America with complex topography and gradients, such a coarse spatial resolution is not necessarily sufficient to determine the snowfall coverage at each specific <sup>10</sup>Be sample site. Therefore, we perform a sensitivity test using data from the Snow Telemetry (SNOTEL) network (USDA Natural Resources Conservation Service, 2021). SNOTEL sites are more accurate measures of local snowfall and snow density but are not evenly distributed across our study area. Interpolating the SNOTEL data across the entire western North America leads to large spatial biases and significant errors for regions with few to no SNOTEL station data. Therefore, for our sensitivity test we choose SNOTEL stations within a 10-km radius and within 150 m of elevation to our <sup>10</sup>Be dataset and that have monthly mean snow depth and snow density data from 1991 to 2020. Based on these criteria we are left with 165 10Be samples that are adjacent to these sites.

From this sample dataset we use the data from that SNOTEL site to calculate the corrected age for the corresponding <sup>10</sup>Be sample applying the LSDn scaling to Equations (2) and (4). If more than one SNOTEL site exists within this search range, the data from the one closest to the sample are used. We then compare the snow depth, snow density, and recalculated age data for these samples based on SNOTEL and the modern reanalysis snow data. Overall, the SNOTEL data demonstrate higher snow depth and density values than the reanalysis data (Fig. 6). After recalculating the ages, the SNOTEL corrected data are older than the reanalysis data on average by 1.5% under the non-wind sweeping

scenario and 2.7% under the wind-swept scenario (Fig. 7). Based on this sensitivity test, the reanalysis data appear to smooth the snow depth and density because of the coarse gridding. Snow depths and densities are lowered by the reanalysis data for samples at higher elevations, while they are raised by the reanalysis data for samples at lower elevations in this dataset. In macroscopic terms, the snow shielding calculated from the reanalysis data is conservative compared to that calculated from the SNOTEL data, but the difference in terms of the correction to the cosmogenic dates is largely indistinguishable within the age uncertainties.

For our snow modeling exercise with the CCSM3 climate output, we calculate snow depth from the climate model assuming a constant Snow To Liquid Ratio (SLR) of 10:1, which is a simplified assumption and likely alters through changes in temperature and moisture source locations (Baxter et al., 2005). The presence of some major prehistorical lakes in the western North America, like Lake Bonneville and Lake Lahontan, are known to have influenced regional snow patterns during their lifespans (e.g. Hostetler et al., 1994), but are not incorporated into this study. Accordingly, climate model choice can influence the simulated history of snow accumulation and coverage, however, the model we use is a downscaled version (Lorenz et al., 2016) of CCSM3 (He, 2011) which was shown to agree with LGM and last deglaciation precipitation proxies across western North America (Oster et al., 2015), giving confidence to the reconstructed historical snow patterns used in this study.

The raw climate model can provide monthly snow precipitation data, but cannot discern the snow accumulation across months or snow melting, therefore we utilize a PDD model (Blard et al., 2007) to incorporate snow accumulation and melting into our analysis. However, we acknowledge that there are limitations preventing the PDD model from being a precise representation of snowfall conditions across our entire domain. For example, we choose a single snow DDF value (Eq. (3)) for our PDD calculation despite spatial variability in this value today (Hock, 1999, 2003), which may under- and overestimate the melting in some locations. Using a distributed PDD model may be advantageous, but given the vast spatial range of our data and the coarse resolution of the climate model output, distributed degree day factors may be of

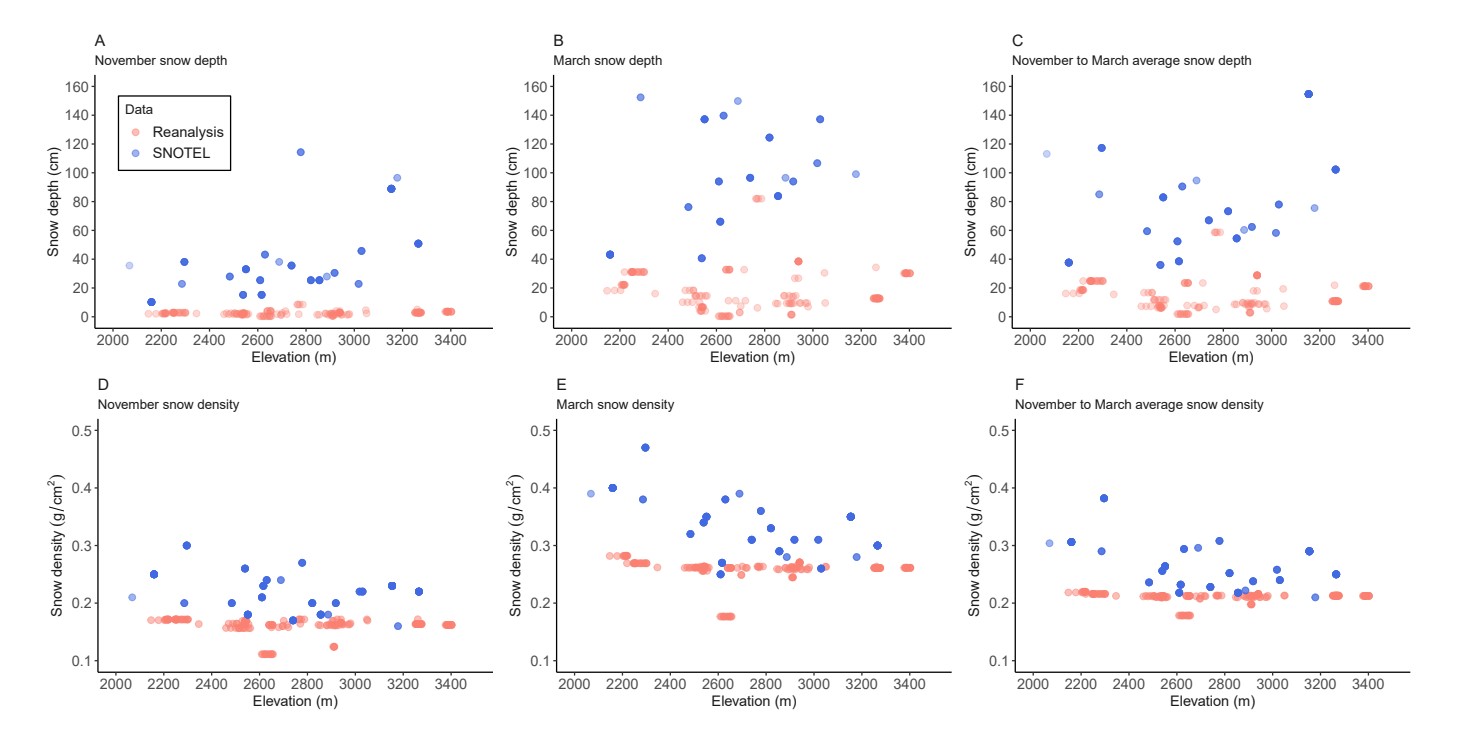
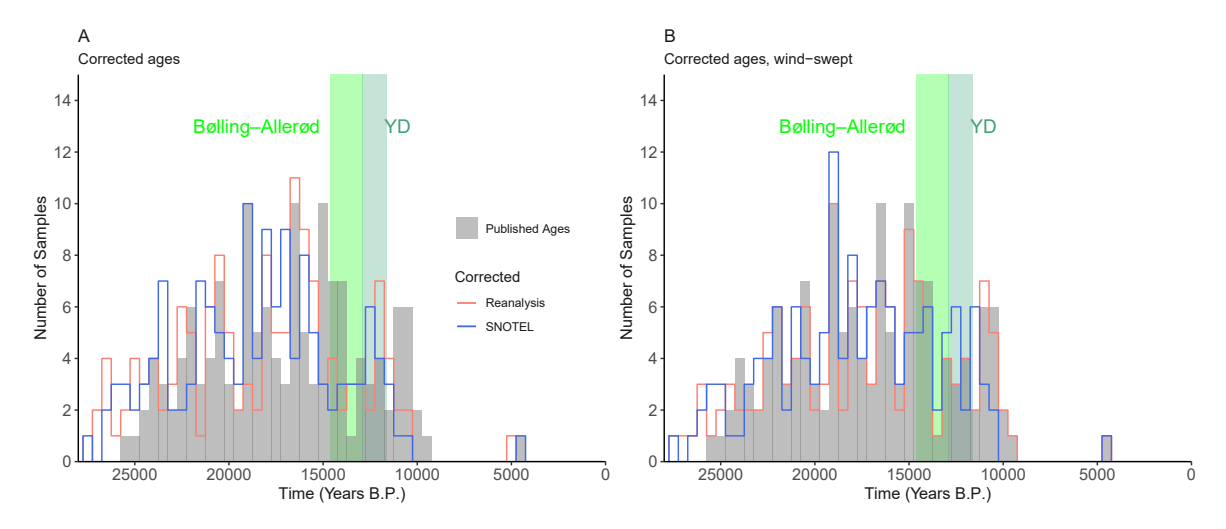


Fig. 6. Comparisons between reanalysis (red) and co-located SNOTEL (blue) data of snow depths (A: November; B: March; C: November–March average) and density (D: November; E: March; F: November–March average).



**Fig. 7.** Published and recalculated ages of the 165  $^{10}$ Be samples with at least one co-located SNOTEL site (A: no wind-sweeping; B: wind-sweept). Green vertical bars demarcate the Bølling-Allerød and Younger Dryas (YD) periods.

limited utility for this modeling exercise. Our choice of SLR and snow density values for the PDD model likely also influence the results of our study. We use a SLR of 10:1 for the fresh snow at all locations, but spatial heterogeneity in these values is known. Baxter et al. (2005) illustrates that the annual mean SLR in the modern western United States could vary from 16:1 in Montana to about 6:1 in coastal California. Density data from the snow reanalysis dataset (Brown and Brasnett, 2020) are based on the month and geographic location of the sample site. Generally, 'old snow' in spring and early summer (e.g.  $> 0.3 \text{ g/cm}^3$  in May for taiga settings) is denser than 'fresh snow' in fall (0.16 g/cm<sup>3</sup> in October and 0.18 g/cm<sup>3</sup> in November for taiga settings). Ephemeral snow, which is usually single snowfall events that melt away quickly, has a higher density (0.3 g/cm<sup>3</sup> in November) (Sturm et al., 1995; Brown and Brasnett, 2020). In other geographic settings, tundra snow has the highest mean density (e.g. 0.21 g/cm<sup>3</sup> in November) followed by alpine, maritime and taiga snows (around 0.18 g/cm<sup>3</sup> in November). Snow in the prairie setting generally has the lowest density (0.16 g/cm<sup>3</sup> in November) (Sturm et al., 1995; Brown and Brasnett, 2020). Since our study only focuses on the general trend over a large area, we use an average value of 0.25 g/cm<sup>3</sup> based on the reanalysis data and measured snow density at SNOTEL sites that are close to our sample sites.

Another limitation of this study is that we did not include the snow history at production rates calibration sites in our model exercise. Age adjustments in Table 2 would likely be reduced if the snow cover at the production rate calibration sites was taken into account. Calibration sites and other sample sites may have experienced similar snow cover throughout the history, and this would reduce the amount of correction for exposure age. This was beyond the scope of this study but future work could incorporate this into the final analyses.

Ultimately, the reconstructed snow patterns used here only illustrate the potential influence on snow shielding when considering historical snow changes and are not intended to be an absolute quantitative metric for applying corrections to ages. Our assumptions on the wind-sweeping effects and the snow density calculations for the historical data also contribute to uncertainties within our analyses. In addition to wind sweeping, the influence of albedo could be another factor that minimizes the impact of snow cover on exposure ages. Boulders have a much lower albedo than snow, and this tends to reduce the amount and duration of snowpack that persists on the boulder tops. Other considerations of topography, boulder orientation, and historical wind patterns, all of which could potentially influence the snow property and wind-sweeping scenario, are not considered in this study. However, from this study a general picture of the spatiotemporal variabilities of the snow shielding effects across western North America is illustrated in a consistent

framework, which agrees with more locally based analyses. Accordingly, the effects of snow shielding are highlighted using several scenarios to provide general estimates of the effects of snow shielding on cosmogenic surface exposure ages across complex geography where several thousands of dates now exist. Although this study focuses on the effect of snow shielding in age calculation, it would also be worthwhile to have the snow shielding included in the calibrated production rates for sites where the snow cover has been deep enough to affect the production.

#### 5. Conclusions

We present a synthesis of snow and <sup>10</sup>Be data across western North America to illustrate the importance of snow shielding in cosmogenic nuclide dating in complex topographic terrains. We find that snow shielding can significantly influence the exposure age estimates, and the spatial and temporal variation of snow cover plays an important role in determining the calculated ages. For example, when considering the time-integrated snow data, the age of an LGM sample in the Sierra Nevada of California could be shifted by almost 17.8% but only 3.5% in the Great Basin when no wind-sweeping is assumed. Also, we find that the modern snow cover data are not representative enough for calculating the snow factor in western North America during the latest Pleistocene since the snow pattern and accumulation has changed significantly through time, with snow-corrected ages calculated from the modern data differing from those calculated using time-integrated data by up to 20% (for different wind-sweeping scenarios). Assumptions of wind-sweeping of snow cover also have large implications where  $^{10}\mathrm{Be}$  ages under wind-swept and non-wind-swept scenarios can differ by 7.6% on average for LGM samples. These analyses provide a first-order quantification of the spatiotemporal variability and complexity of snow shielding effects on surface exposure dates across western North America and further highlights the need to consider snow depth variations both spatially and temporally when conducting surface exposure dating in complex topographic terrains.

#### Declaration of competing interest

The authors declare that they have no known competing financial interests or personal relationships that could have appeared to influence the work reported in this paper.

#### Data availability

The <sup>10</sup>Be dataset and time-integrated snow correction factors calculated in this study are available on the GitHub repository: https://github.

com/yeshancqcq/snow\_sheilding\_correction\_factors\_western\_NAm. The <sup>10</sup>Be data are also hosted on the Sparrow database (https://sparrow-data.org/).

#### Acknowledgments

This work was funded in part by a National Science Foundation EARTHCUBE grant, EAR-1740694 (to S.A.M.) and a Climate People and Environment Program Reid Bryson grant (to S.A.M.). We thank Eric Leonard, Benjamin Laabs, Christopher Darvill, Brendon Quirk, Dennis Dahms, Markus Egli, and Keith Brugger for providing data, Greg Balco for discussions and maintaining the ALPINE ICE-D database (htt p://www.ice-d.org/), and Romain Delunel, an anonymous reviewer, and editor Pierre-Henri Blard for constructive reviews that significantly improved the manuscript.

#### References

- Amaya, Dillon J., et al., 2022. Air-sea coupling shapes North American hydroclimate response to ice sheets during the Last Glacial Maximum. Earth Planet Sci. Lett. 578, 117271
- Amos, Colin B., et al., 2010. Late quaternary slip rate on the kern canyon fault at soda spring, tulare county, California. Lithosphere 2 (6), 411–417.
- Balbas, Andrea M., et al., 2017. 10Be dating of late Pleistocene megafloods and Cordilleran Ice Sheet retreat in the northwestern United States. Geology 45 (7), 583–586.
- Balco, Greg, et al., 2008. A complete and easily accessible means of calculating surface exposure ages or erosion rates from 10Be and 26Al measurements. Quat. Geochronol. 3 (3), 174–195.
- Balco, Greg, 2011. Contributions and unrealized potential contributions of cosmogenicnuclide exposure dating to glacier chronology, 1990–2010. Quat. Sci. Rev. 30, 1–2, 3-27.
- Baxter, Martin A., Graves, Charles E., Moore, James T., 2005. A climatology of snow-to-liquid ratio for the contiguous United States. Weather Forecast. 20 (5), 729–744.
- Becker, R.A., Barth, A.M., Marcott, S.A., Tikoff, B., Caffee, M., 2018a. The last deglaciation along mono creek and the south fork of the san joaquin river, Sierra Nevada, USA. In: Becker, R.A. (Ed.), Glacial Geology and Geomorphology of the West-Central Sierra Nevada. PhD thesis, University of Wisconsin-Madison, USA.
- Becker, R.A., Marcott, S.A., Tikoff, B., Caffee, M., 2018b. Rate and timing of the last deglaciation in tuolumne meadows and lyell canyon, yosemite national park, USA In: Becker, R.A. (Ed.), Glacial Geology and Geomorphology of the West-Central Sierra Nevada. PhD thesis, University of Wisconsin-Madison, USA.
- Benn, Douglas I., et al., 2006. Pleistocene lake outburst floods and fan formation along the eastern Sierra Nevada, California: implications for the interpretation of intermontane lacustrine records. Quat. Sci. Rev. 25 (21–22), 2729–2748.
- Benson, Larry, et al., 2004. The probable importance of snow and sediment shielding on cosmogenic ages of north-central Colorado Pinedale and pre-Pinedale moraines. Quat. Sci. Rev. 23 (1–2), 193–206.
- Benson, Larry, et al., 2007. Surface-exposure ages of front range moraines that may have formed during the younger Dryas, 8.2 cal ka, and little ice age events. Quat. Sci. Rev. 26 (11–12), 1638–1649.
- Blard, P.H., et al., 2007. Persistence of full glacial conditions in the central Pacific until 15,000 years ago. Nature 449, 591–594, 7162.
- Brasnett, Bruce, 1999. A global analysis of snow depth for numerical weather prediction. J. Appl. Meteorol. 38 (6), 726–740.
- Breckenridge, Roy, Phillips, W.M., 2010. New cosmogenic 10Be surface exposure ages for the Purcell Trench lobe of the Cordilleran ice sheet in Idaho. Geol. Soc. Am. Abstracts Programs 42, 309.
- Briner, Jason P., 2009. Moraine pebbles and boulders yield indistinguishable 10Be ages: a case study from Colorado, USA. Quat. Geochronol. 4 (4), 299–305.
- Bromwich, David H., et al., 2004. Polar MM5 simulations of the winter climate of the Laurentide ice sheet at the LGM. J. Clim. 17 (17), 3415–3433.
- Brown, L., 1987. 10Be: recent applications in Earth sciences. Phil. Trans. Roy. Soc. Lond. Math. Phys. Sci. 323 (1569), 75–86.
- Brown, R.D., Brasnett, B., 2020. Canadian Meteorological Centre (CMC) Daily Snow Depth Analysis Data, Version 1. updated annually. NASA National Snow and Ice Data Center Distributed Active Archive Center, Boulder, Colorado USA. https://doi.org/10.5067/W9FOYWH0EQZ3. (Accessed 1 February 2022).
- Brugger, Keith A., 2007. Cosmogenic 10Be and 36Cl ages from Late Pleistocene terminal moraine complexes in the Taylor River drainage basin, central Colorado, USA. Quat. Sci. Rev. 26 (3–4), 494–499.
- Brugger, Keith A., et al., 2019a. Late Pleistocene glaciation in the mosquito range, Colorado, USA: chronology and climate. J. Quat. Sci. 34 (3), 187–202.

- Brugger, Keith A., et al., 2019b. Climate during the last glacial maximum in the northern Sawatch range, Colorado, USA. Quaternary 2 (4), 36.
- Bush, Andrew BG., Philander, S. George H., 1999. The climate of the Last Glacial Maximum: results from a coupled atmosphere-ocean general circulation model. J. Geophys. Res. Atmos. 104 (D20), 24509–24525.
- Cehak-Trock, 1957. Herta. "Der feste Niederschlag im atlantischen Klimagebiet. Archiv für Meteorologie, Geophysik und Bioklimatologie, Serie B 8 (3), 352–368.
- Chenet, Marie, et al., 2016. 10Be cosmic-ray exposure dating of moraines and rock avalanches in the Upper Romanche valley (French Alps): evidence of two glacial advances during the Late Glacial/Holocene transition. Quat. Sci. Rev. 148, 209–221.
- Chmeleff, Jérôme, et al., 2010. Determination of the 10Be half-life by multicollector ICP-MS and liquid scintillation counting. Nuclear Instruments and Methods in Physics Research Section B: Beam Interactions with Materials and Atoms 268, 192–199.
- Collins, William D., et al., 2006. The community climate system model version 3 (CCSM3). J. Clim. 19 (11), 2122–2143.
- Dahms, Dennis, et al., 2018. Revised Quaternary glacial succession and post-LGM recession, southern Wind River Range, Wyoming, USA. Quat. Sci. Rev. 192, 167–184.
- Dahms, Dennis E., 2004. Relative and numeric age data for Pleistocene glacial deposits and diamictons in and near Sinks Canyon, Wind River Range, Wyoming, USA. Arctic Antarct. Alpine Res. 36 (1), 59–77.
- Darvill, C.M., et al., 2018. Retreat of the western Cordilleran Ice Sheet margin during the last deglaciation. Geophys. Res. Lett. 45 (18), 9710–9720.
- Delunel, Romain, et al., 2014. Snow shielding factors for cosmogenic nuclide dating inferred from long-term neutron detector monitoring. Quat. Geochronol. 24, 16–26.
- Delunel, Romain, et al., 2020. Late-Pleistocene catchment-wide denudation patterns across the European Alps. Earth Sci. Rev. 211, 103407.
- Dubé-Loubert, Hugo, et al., 2018. 10Be dating of former glacial Lake Naskaupi (Québec-Labrador) and timing of its discharges during the last deglaciation. Quat. Sci. Rev. 191, 31–40.
- Dühnforth, Miriam, Anderson, Robert S., 2011. Reconstructing the glacial history of green lakes valley, north boulder creek, Colorado front range. Arctic Antarct. Alpine Res. 43 (4), 527–542.
- Dühnforth, Miriam, et al., 2010. Bedrock fracture control of glacial erosion processes and rates. Geology 38 (5), 423–426.
- Dulfer, Helen E., et al., 2021. Using 10Be dating to determine when the cordilleran ice sheet stopped flowing over the Canadian Rocky mountains. Quat. Res. 102, 222–233.
- Egli, Markus, et al., 2020. Landscape Evolution, Post-LGM Surface Denudation and Soil Weathering Processes from Dickinson Park Mire, Wind River Range, Wyoming (USA), vol. 371. Geomorphology, 107433.
- Fabel, Derek, et al., 2004. Spatial patterns of glacial erosion at a valley scale derived from terrestrial cosmogenic 10Be and 26Al concentrations in rock. Ann. Assoc. Am. Geogr. 94 (2), 241–255.
- Fleming, Kaitlyn, 2019. Cosmogenic 10 Be Surface Exposure Dating and Numerical Modeling of Late Pleistocene Glaciers and Lakes in Northwestern Nevada. Diss. North Dakota State University.
- Getis, Arthur, Keith Ord, J., 2010. The Analysis of Spatial Association by Use of Distance statistics." *Perspectives On Spatial Data Analysis*. Springer, Berlin, Heidelberg, pp. 127–145.
- Gosse, John C., et al., 1995a. Precise cosmogenic 10Be measurements in western North America: support for a global Younger Dryas cooling event. Geology 23 (10), 877–880.
- Gosse, John C., et al., 1995b. Beryllium-10 dating of the duration and retreat of the last Pinedale glacial sequence. Science 268 (5215), 1329–1333.
- Gosse, John C., Phillips, Fred M., 2001. Terrestrial in situ cosmogenic nuclides: theory and application. Ouat. Sci. Rev. 20 (14), 1475–1560.
- Guido, Zackry S., Ward, Dylan J., Anderson, Robert S., 2007. Pacing the post–last glacial maximum demise of the animas valley glacier and the san juan mountain ice cap, Colorado. Geology 35 (8), 739–742.
- Hancock, Gregory S., et al., 1999. Dating fluvial terraces with 10Be and 26Al profiles: application to the wind river, Wyoming. Geomorphology 27 (1–2), 41–60.
- He, Feng, 2011. Simulating transient climate evolution of the last deglaciation with CCSM 3 72 (10).
- Heyman, Jakob, et al., 2016. Boulder height–exposure age relationships from a global glacial 10Be compilation. Quat. Geochronol. 34, 1–11.
- Hippe, Kristina, et al., 2014. Chronology of Lateglacial ice flow reorganization and deglaciation in the Gotthard Pass area, Central Swiss Alps, based on cosmogenic 10Be and in situ 14C. Quat. Geochronol. 19, 14–26.
- Hippolyte, Jean-Claude, et al., 2009. Cosmogenic 10Be dating of a acking and its faulted rock glaciers, in the Alps of Savoy (France). Geomorphology 108 (3–4), 312–320.
- Hock, Regine, 1999. A distributed temperature-index ice-and snowmelt model including potential direct solar radiation. J. Glaciol. 45 (149), 101–111.
- Hock, Regine, 2003. Temperature index melt modelling in mountain areas. J. Hydrol. 282 (1–4), 104–115.
- Hormes, Anne, et al., 2008. 10Be exposure ages of a rock avalanche and a late glacial moraine in Alta Valtellina, Italian Alps. Quat. Int. 190 (1), 136–145.
- Hostetler, S.W., et al., 1994. Lake-atmosphere feedbacks associated with paleolakes Bonneville and Lahontan. Science 263 (5147), 665–668.
- Howle, James F., et al., 2012. Airborne LiDAR analysis and geochronology of faulted glacial moraines in the Tahoe-Sierra frontal fault zone reveal substantial seismic hazards in the Lake Tahoe region. California-Nevada, USA." *Bulletin* 124 (7–8), 1087–1101.
- Ivy-Ochs, Susan, Kober, Florian, 2008. Surface exposure dating with cosmogenic nuclides. E&G Quaternary Sci. J. 57 (1/2), 179–209.

- Ivy-Ochs, Susan, et al., 1999. Moraine exposure dates imply synchronous Younger Dryas glacier advances in the European Alps and in the Southern Alps of New Zealand. Geogr. Ann. Phys. Geogr. 81 (2), 313–323.
- Kohut, Daryl Lee, 2011. Glacial Chronology of a High Altitude Moraine Series, Tamarack Bench/Francis Canyon, Sierra Nevada. California. University of California, Riverside.
- Korschinek, Gunther, et al., 2010. A new value for the half-life of 10Be by heavy-ion elastic recoil detection and liquid scintillation counting. Nuclear Instruments and Methods in Physics Research Section B: Beam Interactions with Materials and Atoms 268 (2), 187–191.
- Krasting, John P., et al., 2013. Future changes in northern Hemisphere snowfall. J. Clim. 26 (20), 7813–7828.
- Kutzbach, John E., 1987. Model simulations of the climatic patterns during the deglaciation of North America. North America and adjacent oceans during the last deglaciation 3, 425–446.
- Laabs, Benjamin J., et al., 2020. Updated cosmogenic chronologies of Pleistocene mountain glaciation in the western United States and associated paleoclimate inferences. Quat. Sci. Rev. 242, 106427.
- Laabs, Benjamin J., et al., 2011. Chronology of latest Pleistocene mountain glaciation in the western Wasatch Mountains, Utah, USA. Quat. Res. 76 (2), 272–284.
- Laabs, Benjamin J., Munroe, J.S., 2016. Late Pleistocene mountain glaciation in the Lake Bonneville basin. Dev. Earth Surf. Process 20, 462–503. Elsevier.
- Laabs, Benjamin J., et al., 2013. Timing of the last glaciation and subsequent deglaciation in the ruby mountains, Great Basin, USA. Earth Planet Sci. Lett. 361, 16–25
- Laabs, Benjamin J., et al., 2007. Chronology of the last glacial maximum in the upper Bear River basin, Utah. Arctic Antarct. Alpine Res. 39 (4), 537–548.
- Laabs, Benjamin J., et al., 2009. Latest Pleistocene glacial chronology of the Uinta Mountains: support for moisture-driven asynchrony of the last deglaciation. Quat. Sci. Rev. 28 (13–14), 1171–1187.
- Lal, Devendra, Peters, B., 1967. Cosmic Ray Produced Radioactivity on the Earth." Kosmische Strahlung II/Cosmic Rays II. Springer, Berlin, Heidelberg, pp. 551–612.
- Lal, Devendra, 1991. Cosmic ray labeling of erosion surfaces: in situ nuclide production rates and erosion models. Earth Planet Sci. Lett. 104 (2-4), 424–439.
- Legates, D.R., 1987. A climatology of global precipitation. Publ. Climatol. 40 (1), 1–85.
  Leonard, Eric M., et al., 2017. Late Pleistocene glaciation and deglaciation in the crestone peaks area, Colorado sangre de Cristo mountains, USA-chronology and paleoclimate. Quat. Sci. Rev. 158, 127–144.
- Licciardi, J.M., et al., 1999. Calibration of cosmogenic 3He production rates from Holocene lava flows in Oregon, USA, and effects of the Earth's magnetic field. Earth Planet Sci. Lett. 172 (3-4), 261–271.
- Licciardi, Joseph M., et al., 2004. Variable responses of western US glaciers during the last deglaciation. Geology 32 (1), 81–84.
- Licciardi, Joseph M., et al., 2001. Cosmogenic 3He and 10Be chronologies of the late Pinedale northern Yellowstone ice cap, Montana, USA. Geology 29 (12), 1095–1098.
- Licciardi, Joseph M., Pierce, Kenneth L., 2008. Cosmogenic exposure-age chronologies of Pinedale and bull lake glaciations in greater yellowstone and the teton range, USA. Quat. Sci. Rev. 27 (7–8), 814–831.
- Licciardi, Joseph M., Pierce, Kenneth L., 2018. History and dynamics of the greater yellowstone glacial system during the last two glaciations. Quat. Sci. Rev. 200, 1–33.
- Lifton, Nathaniel A., et al., 2005. Addressing solar modulation and long-term uncertainties in scaling secondary cosmic rays for in situ cosmogenic nuclide applications. Earth Planet Sci. Lett. 239 (1–2), 140–161.
- Liu, Zhengyu, et al., 2009. Transient simulation of last deglaciation with a new mechanism for Bølling-Allerød warming. Science 325 (5938), 310–314.
- Lora, Juan M., Ibarra, Daniel E., 2019. The North American hydrologic cycle through the last deglaciation. Quat. Sci. Rev. 226, 105991.
- Lorenz, David J., et al., 2016. Downscaled and debiased climate simulations for North America from 21,000 years ago to 2100AD. Sci. Data 3 (1), 1–19.
- Mahan, Shannon A., et al., 2014. A geochronologic framework for the Ziegler Reservoir fossil site, Snowmass Village, Colorado. Quat. Res. 82 (3), 490–503.
- Marcott, Shaun A., et al., 2019. 10Be age constraints on latest Pleistocene and Holocene cirque glaciation across the western United States. Npj Clim. Atmosp. Sci. 2 (1), 1–7.
- Margold, Martin, et al., 2014. Timing of terminal Pleistocene deglaciation at high elevations in southern and central British Columbia constrained by 10Be exposure dating. Quat. Sci. Rev. 99, 193–202.
- Margold, Martin, et al., 2019. Beryllium-10 dating of the foothills erratics train in alberta, Canada, indicates detachment of the Laurentide ice sheet from the Rocky mountains at  $\sim 15$  ka. Quat. Res. 92 (2), 469–482.
- McGee, David, et al., 2018. Western US lake expansions during Heinrich stadials linked to Pacific Hadley circulation. Sci. Adv. 4, eaav0118, 11.
- Menounos, Brian, et al., 2013. Did rock avalanche deposits modulate the late Holocene advance of Tiedemann Glacier, southern Coast Mountains, British Columbia, Canada? Earth Planet Sci. Lett. 384, 154–164.
- Menounos, Brian, et al., 2017. Cordilleran Ice Sheet mass loss preceded climate reversals near the Pleistocene Termination. Science 358 (6364), 781–784.

- Morris, Julie D., 1991. Applications of cosmogenic 10Be to problems in the earth sciences. Annu. Rev. Earth Planet Sci. 19 (1), 313–350.
- Munroe, Jeffrey S., et al., 2006. Latest Pleistocene advance of alpine glaciers in the southwestern Uinta Mountains, Utah, USA: evidence for the influence of local moisture sources. Geology 34 (10), 841–844.
- Nishiizumi, Kunihiko, et al., 2007. Absolute calibration of 10Be AMS standards. Nucl. Instrum. Methods Phys. Res. Sect. B Beam Interact. Mater. Atoms 258 (2), 403–413.
- Nishiizumi, K., et al., 1993. Role of in situ cosmogenic nuclides 10Be and 26Al in the study of diverse geomorphic processes. Earth Surf. Process. Landforms 18 (5), 407–425.
- Nishiizumi, K., et al., 1989. Cosmic ray production rates of 10Be and 26Al in quartz from glacially polished rocks. J. Geophys. Res. Solid Earth 94 (B12), 17907–17915.
- Oster, Jessica L., et al., 2015. Steering of westerly storms over western North America at the last glacial maximum. Nat. Geosci. 8 (3), 201–205.
- Owen, Lewis A., et al., 2003. Extreme southwestern margin of late Quaternary glaciation in North America: timing and controls. Geology 31 (8), 729–732.
- Phillips, Fred M., et al., 1997. Cosmogenic 36Cl and 10Be ages of quaternary glacial and fluvial deposits of the wind river range, Wyoming. Geol. Soc. Am. Bull. 109 (11), 1453–1463.
- Phillips, William M., et al., 2006. Cosmogenic 10Be and 26Al exposure ages of tors and erratics, Cairngorm Mountains, Scotland: timescales for the development of a classic landscape of selective linear glacial erosion. Geomorphology 73 (3-4), 222–245.
- Pierce, Ian KD., Wesnousky, Steven G., Owen, Lewis A., 2017. Terrestrial cosmogenic surface exposure dating of moraines at Lake Tahoe in the Sierra Nevada of California and slip rate estimate for the West Tahoe Fault. Geomorphology 298, 63–71.
- Quirk, Brendon J., et al., 2018. Termination II, last glacial maximum, and lateglacial chronologies and paleoclimate from Big Cottonwood Canyon, Wasatch Mountains, Utah. Bulletin 130 (11–12), 1889–1902.
- Quirk, Brendon J., et al., 2020. Latest Pleistocene glacial and climate history of the Wasatch range, Utah. Quat. Sci. Rev. 238, 106313.
- Refsnider, Kurt A., et al., 2008. Last glacial maximum climate inferences from cosmogenic dating and glacier modeling of the western Uinta ice field, Uinta Mountains, Utah. Ouat. Res. 69 (1), 130–144.
- Rawlins, Michael A., et al., 2006. Evaluation of trends in derived snowfall and rainfall across Eurasia and linkages with discharge to the Arctic Ocean. Geophys. Res. Lett. 33 (7).
- Rood, Dylan H., Burbank, Douglas W., Finkel, Robert C., 2011. Chronology of glaciations in the Sierra Nevada, California, from 10Be surface exposure dating. Quat. Sci. Rev. 30 (5–6), 646–661.
- Ruleman, Chester A., et al., 2018. Geologic Map of the Leadville North 7.5' quadrangle, Eagle and Lake Counties. Colorado. No. 3400. US Geological Survey.
- Schaefer, Joerg M., et al., 2006. Near-synchronous interhemispheric termination of the last glacial maximum in mid-latitudes. *Science*312 5779, 1510–1513.
- Schildgen, T.F., 2000. Fire and Ice: the Geomorphic History of Middle Boulder Creek as Determined by Isotopic Dating Techniques, Colorado Front Range. Diss. Honors thesis, Williams College, Williamstown, MA.
- Schildgen, T.F., Phillips, W.M., Purves, R.S., 2005. Simulation of snow shielding corrections for cosmogenic nuclide surface exposure studies. Geomorphology 64 (1–2), 67–85.
- Schweinsberg, Avriel D., et al., 2020. Cosmogenic 10Be exposure dating of bull lake and Pinedale moraine sequences in the upper Arkansas river valley, Colorado Rocky mountains, USA. Quat. Res. 97, 125–139.
- Sturm, Matthew, Holmgren, Jon, Glen, E., Liston, 1995. A seasonal snow cover classification system for local to global applications. J. Clim. 8 (5), 1261–1283.
- Tranel, Lisa M., et al., 2015. Quantifying variable erosion rates to understand the coupling of surface processes in the Teton Range, Wyoming. Geomorphology 228, 409–420.
- Tranel, Lisa M., Strow, Meredith L., 2017. 10Be analysis of amalgamated talus pebbles to investigate alpine erosion, Garnet Canyon, Teton Range, Wyoming. Geosphere 13 (1), 36–48.
- Tulenko, Joseph P., et al., 2020. Delayed and rapid deglaciation of alpine valleys in the Sawatch Range, southern Rocky Mountains, USA. Geochronology 2 (2), 245–255.
- USDA Natural Resources Conservation Service, 2021. SNOwpack TELemetry network (SNOTEL). NRCS. https://data.nal.usda.gov/dataset/snowpack-telemetry-network-snotel. (Accessed 3 May 2022). Accessed.
- Ward, Dylan J., et al., 2009. Numerical modeling of cosmogenic deglaciation records, Front Range and San Juan mountains, Colorado. J. Geophys. Res.: Earth Surf. 114 (F1).
- Wesnousky, Steven G., et al., 2016. Terrestrial cosmogenic surface exposure dating of glacial and associated landforms in the Ruby Mountains-East Humboldt Range of central Nevada and along the northeastern flank of the Sierra Nevada. Geomorphology 268, 72–81.
- Young, Nicolás E., et al., 2011. Assessing climatic and nonclimatic forcing of Pinedale glaciation and deglaciation in the western United States. Geology 39 (2), 171–174.